IVYSPRING INTERNATIONAL PUBLISHER

Theranostics

2027; 17(1): 573-588. doi: 10.7150/thno.139857

Research Paper

Targeted delivery of selenomethionine by RGD-functionalized liposomes inhibits AAD progression through dual modulation of inflammation and BRD4 lactylation

Jiamin Xu[1#], Xi Tan[2#], Ke Hu[5#], Xu Zhou[1#], Xiaohan Fan[3], Lihua Tian[1], Heng Wu[1], Zhongnan Xia[1], Ya Wang[1], Xuemei Zhang[1], Changzhao Liu[1], Hongbo Chen[1], Lixing Wu[2]✉, Yuhua Lei[1]✉, Jing Zhang[3]✉, Jiaxin Hu[1,4,6]✉

1. Cardiovascular Disease Center, Hubei Key Laboratory for Translational Research in Traditional Chinese Medicine, The Central Hospital of Enshi Tujia and Miao Autonomous Prefecture, Enshi, 445000, Hubei Province, China.
2. Department of Cardiology, Affiliated Hospital of Integrated Traditional Chinese and Western Medicine, Nanjing University of Chinese Medicine, Nanjing, China.
3. State Key Laboratory of Materials-Oriented Chemical Engineering, College of Chemical Engineering, Nanjing Tech University, 30 Puzhu South Road, Nanjing, 211816 China.
4. Hubei Key Laboratory for Translational Research in Traditional Chinese Medicine, the Central Hospital of Enshi Tujia and Miao Autonomous Prefecture, Hubei Minzu University, China.
5. Department of Cardiology, The Second Xiangya Hospital, Central South University, Changsha, Hunan, China.
6. The People's Hospital of JianShi,Jianshi, Hubei Province, China.

#Jiamin Xu, Xi Tan, Ke Hu and Xu Zhou contributed equally to this work.

✉ Corresponding authors: Jiaxin Hu: Cardiovascular Disease Center, The Central Hospital of Enshi Tujia and Miao Autonomous Prefecture, Enshi Clinical College of Wuhan University, No.158 Wuyang Avenue, Enshi, Hubei, China; E-mail: hujiaxin_esch@hbmzu.edu.cn. Jing Zhang: State Key Laboratory of Materials-Oriented Chemical Engineering, College of Chemical Engineering, Nanjing Tech University, 5 Xin Mofan Road, Nanjing 210009, PR China; E-mail:jing.zhang@njtech.edu.cn. Yuhua Lei: Cardiovascular Disease Center, The Central Hospital of Enshi Tujia and Miao Autonomous Prefecture, Enshi Clinical College of Wuhan University, No.158 Wuyang Avenue, Enshi, Hubei, China; Email: lyh-xnk@outlook.com. Lixing Wu: Department of Cardiology, Affiliated Hospital of Integrated Traditional Chinese and Western Medicine, Nanjing University of Chinese Medicine, Nanjing, China; Email: wulixing@jsatcm.com.

© 2027 The Author(s). This is an open access article distributed under the Creative Commons Attribution 4.0 International Licence, subject to the Publisher's Terms of Use at https://ivyspring.com/terms.

Received: 2026.06.25; Accepted: 2026.10.09; Published: 2027.01.01

Abstract

Rationale: Effective pharmacological treatments for aortic aneurysm and dissection (AAD) remain unavailable. Selenium deficiency is associated with increased AAD risk, but the narrow therapeutic window of conventional selenium agents limits their clinical translation. Thus, we constructed a novel RGD-modified liposomal delivery system for targeted selenomethionine (SeMet) delivery to aortic lesion tissues.

Methods: We constructed RGD-functionalized liposomes loaded with SeMet (termed SeMet-LP@RGD) that specifically bind to integrin αvβ3, which is highly expressed on pro-inflammatory M1 macrophages and pathological synthetic vascular smooth muscle cells (VSMCs) in AAD lesions. The targeting enrichment capability, biosafety, and *in vivo* therapeutic efficacy of SeMet-LP@RGD were systematically validated in both β-aminopropionitrile (BAPN)-induced thoracic aortic dissection and angiotensin II (AngII)-induced abdominal aortic aneurysm mouse models. A combination of multi-omics analysis, molecular biological experiments, and gene mutation verification was further applied to explore the underlying therapeutic mechanisms.

Results: SeMet-LP@RGD exhibited excellent targeted accumulation in aortic lesion cells and effectively reduced aortic medial injury, suppressed aneurysm expansion, and delayed pathological progression of aortic dissection *in vivo*. Mechanistically, SeMet-LP@RGD exerted dual protective effects against AAD. It inhibited excessive activation of the NF-κB signaling pathway in macrophages, thereby reversing M1 pro-inflammatory macrophage polarization and reducing local vascular inflammation. In VSMCs, SeMet-LP@RGD specifically downregulated lactylation at the BRD4 K1234 site, which blocked the pathological transformation of VSMCs from a contractile phenotype to a synthetic phenotype. Benefiting from RGD-mediated active targeting, SeMet-LP@RGD significantly enriched SeMet in diseased aortic tissues, minimized off-target damage to healthy normal tissues, and effectively compensated for the insufficient targeting and low bioavailability of free SeMet.

Conclusions: This study constructs and validates a dual-cell targeted nano-delivery system SeMet-LP@RGD for AAD treatment. The formulation improves the efficacy and safety of SeMet-based therapy via precise lesion targeting, and reveals a novel regulatory mechanism by which BRD4 K1234 lactylation modulates VSMC phenotypic switching. The findings provide robust preclinical evidence for the application of SeMet-LP@RGD as a promising therapeutic candidate for AAD, offering a new strategy for targeted clinical intervention of aortic aneurysm and dissection.

Keywords: aortic aneurysm and dissection, selenomethionine, liposomes, nanotherapeutic

Introduction

Aortic aneurysm presents as a local or generalized aortic enlargement. It is considered an abnormality and a diagnosis, when a vessel is dilated more than 50% from its normal caliber. The disease is associated with a high mortality and accounts for some 170,000 deaths globally every year [1]. In the absence of proper clinical care, patients may still have the risk of rupture, and aortic dissection is one of the most devastating complications [2]. For small asymptomatic aneurysms the current guidance is to have imaging surveillance, with a diameter of 30‑50 mm in female and 30‑55 mm in male. Surgical intervention is indicated if lesions are large, symptomatic and/or if rupture is confirmed [3]. While surgical techniques have advanced, there is no medication that will stop or prevent the aneurysm from rupturing in patients with small aneurysms that do not have symptoms [4]. The risk of unanticipated rupture remains for patients under surveillance [5]. Pharmacological interventions therefore are required that can prevent the development of aneurysm enlargement and lessen the risk of rupture, either alongside surgery or as an alternative treatment choice [6].

Aortic aneurysm and dissection (AAD) are a disease characterized by chronic inflammation, degradation of extracellular matrix (ECM), and dysfunction of vascular smooth muscle cells (VSMCs) [7]. This continuous process of M1 macrophage polarization and phenotypic shift of VSMCs from a contractile phenotype to a synthetic phenotype leads to the remodeling and weakening of the vessel wall [8]. In response to vascular injury or elevated hemodynamic stress, circulating monocytes infiltrate aortic tissue and the tissue microenvironment promotes their polarization to M1 macrophages [9].M1 macrophages secrete IL-6, IL-1β and TNF-α as well as the matrix-degrading MMP-2 and MMP-9. All of these inflammatory mediators and proteases contribute to the degradation of aortic elastin and collagen, thus weakening the vessel wall [10].M1 macrophages also produce reactive oxygen species (ROS), contributing to the oxidative damage and promoting ECM degradation. Persistent inflammation with predominance of M1 therefore facilitates the growth of aneurysm and the risk of rupture [11]. Concurrently, VSMCs become less contractile, with reduced expression of α-SMA, SM-MHC, and calponin-1 and increased expression of vimentin and osteopontin (OPN), synthetic markers. This phenotypic switch further leads to aortic medial thinning and vascular contractility defect, which is known to further promote AAD [12].

In human aortic aneurysm (AA) samples, and in mouse models, single-cell RNA sequencing revealed two pathological features: macrophage polarization to an M1 (pro-inflammatory) state and VSMC loss of the contractile phenotype [13]. Integrin αvβ3 is up regulated in injured aortic tissue in both M1 macrophages and synthetic VSMCs [13]. Hence, targeting this receptor could be a solution for both macrophage and VSMC-mediated inflammation and vessel deterioration. The main anti-inflammatory and antioxidant actions of selenium are related to its inclusion in selenoproteins [14]. Among selenium-based agents, SeMet has shown therapeutic promise [15]. It improves cellular antioxidant protection mechanisms by helping to generate selenocysteine and stabilizes plaques and reparative vascular remodeling [16]. But the general problem of free SeMet lies in the lack of tissue specificity, fast clearance from the blood stream and toxicity to various tissues, which hinder its clinical translation.

We created SeMet-LP@RGD to overcome these delivery restrictions. The formulation is liposomal SeMet incorporating RGD peptides, which are able to bind to integrin αvβ3 within the diseased aortic tissue. This interaction not only guides the carrier to M1 macrophages but also to synthetic VSMCs. Local enrichment enhances the drug concentration and bioavailability at the lesion, and decreases the amount of drug reaching healthy tissues. The formulation can thus have a significant therapeutic activity with lower doses and simultaneously avoid the organ toxicity of high doses of free SeMet. This design not only uses SeMet delivery but also targets two cell types contributing to AAD pathogenesis.

We identified two mechanisms of protection during our experiments. SeMet-LP@RGD inhibited the production of inflammatory cytokines such as IL-6 and IL-1β from macrophages, by inhibiting excess activation of NF-κB and promoting an anti-inflammatory M2-like phenotype. Under the

treatment, the VSMCs regained the contractile properties, among them those of α-SMA expression. Mechanistic analysis revealed that SeMet-LP@RGD selectively reduced BRD4 lactylation at the K1234 residue which stabilized the contractile gene transcriptional program and stalled the synthetic phenotype transition (Figure 1). The results link the pharmacological properties of SeMet to integrin αvβ3-mediated delivery to aortic lesions, offering a precise targeted therapeutic approach to aortic aneurysm and aortic dissection.

Materials and Methods

Detailed experimental methods are provided in the Supporting Information.

Statistical analysis

Data is presented as the mean ± standard error of the mean (SEM). All statistical analyses were performed using GraphPad Prism 9.0 software (GraphPad Software, Inc., San Diego, CA, USA). For comparisons between two groups, an unpaired two-tailed Student's T-test was applied. For comparisons among three or more groups, one-way or two-way analysis of variance (ANOVA) was performed, followed by Tukey's post hoc test for multiple comparisons. A p-value < 0.05 was considered statistically significant. (*p < 0.05, **p < 0.01, ***p < 0.001, ****p < 0.0001; ns, not significant.)

Results

Preparation and characterization of SeMet-LP@RGD

We first measured integrin αvβ3 expression by flow cytometry. Expression was significantly higher in M1 macrophages than in M0 or M2 macrophages and higher in synthetic VSMCs than in contractile VSMCs (Figure S1). We then prepared RGD-modified liposomes for SeMet delivery. Blank liposomes were produced by microfluidic mixing, loaded with SeMet through freeze-thaw cycles, and subsequently conjugated with RGD peptides (Figure 2A). To test the reactivity of surface maleimide groups toward thiols, drug-loaded liposomes were incubated separately with a thiol-containing fluorescent probe (FITC-PEG2k-SH, MW 2000 Da) or a nonreactive control probe (FITC-PEG2k-OH, MW 2000 Da). Both incubations were conducted at pH 7.2 and 37 °C for 1 h, protected from light. After removal of unbound probes, absorbance retention was calculated as post-filtration absorbance divided by pre-filtration absorbance at 490 nm. Stable covalent bond formation between thiol and maleimide groups was confirmed as the retention increased to 74%, which was significantly higher than the −OH control (46%), (Figure S2A). In SD rats, plasma levels of intravenously injected free SeMet

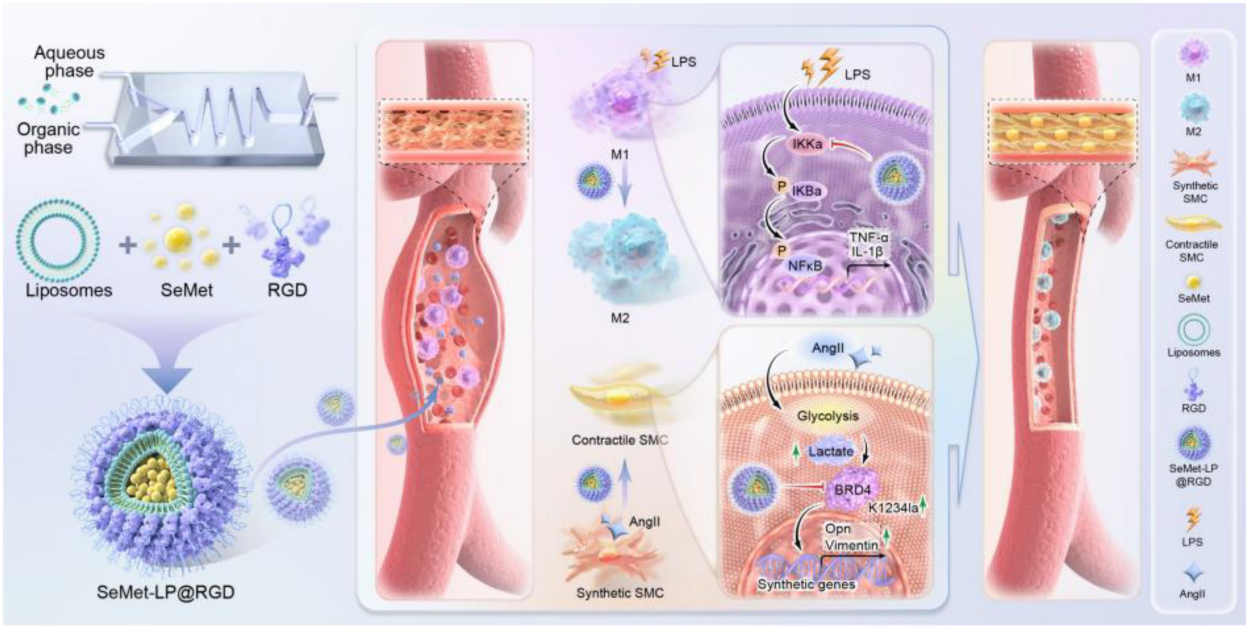


Figure 1. Schematic illustration of the fabrication, targeted delivery, and dual therapeutic mechanisms of SeMet-LP@RGD for AAD treatment. RGD-modified liposomal nanoparticles loaded with SeMet were successfully constructed via microfluidic mixing, extrusion, freeze-thaw drug loading, and peptide conjugation. Owing to the specific binding ability with integrin αvβ3, SeMet-LP@RGD can actively target and accumulate in AAD lesion-resident M1 macrophages and synthetic VSMCs. Mechanistically, SeMet-LP@RGD alleviates vascular inflammatory injury by suppressing NF-κB signaling activation and reversing pro-inflammatory M1 macrophage polarization. In VSMCs, SeMet-LP@RGD downregulates BRD4 lactylation at the K1234 site, thereby inhibiting the pathological transformation of VSMCs from a contractile phenotype to a synthetic phenotype. The dual regulatory effects on inflammation and VSMC phenotypic remodeling ultimately inhibit aortic dilatation and dissection progression, achieving precise and efficient targeted therapy for AAD with reduced systemic side effects.

rapidly decreased over 2h. Plasma SeMet levels remained elevated for a longer duration in SeMet-LP@RGD (Figure S2B). The blank liposomes, after microfluidic mixing (LP), liposomes after extrusion and RGD-conjugated SeMet-loaded liposomes showed no visible precipitation or aggregation based on visual inspection (Figure 2B). TEM images showed that both LP and SeMet-LP particles were spherical, and they were well dispersed uniformly (Figure 2C). The Z-average diameter and the polydispersity index (PDI) of SeMet-LP and SeMet-LP@RGD remained unchanged during 72-h storage at 4° C in the medium at pH 7.4. The mean diameters of these were 106.0± 4.6 nm and 112.5±2.6 nm respectively (Figures 2D-E), in which the small difference was in line with the surface modification with RGD. The encapsulation efficiency obtained by the freeze-thaw loading technique at pH 7.4 was 42.1±5.8%. In the case of SeMet-LP treatment, the same value dropped from ~43% at the start to ~36% at 12h and then slowly increased and reached 35-40% stable range. SeMet-LP@RGD also began at around 43% and fell to around 25% after 12 hours and stayed in that range after that. Thus, the loading efficiency of SeMet was lowered with RGD conjugation, but both formulations showed the presence of encapsulated drug at all time points (Figure 2F). Moreover, SeMet-LP@RGD displayed pH-responsive drug release with accelerated payload leakage under acidic conditions and retained stable particle size and PDI in 10% FBS for at least 7 days, demonstrating favorable colloidal stability (Figure S2C-D). We determined the concentration of SeMet using high-performance liquid chromatography (HPLC) and serial dilutions of reference samples (Figure 2G). Each reference sample gave rise to only one symmetrical peak, which had no discernible tailing at about 2.0 min, indicating good separation and sensitivity of detection at optimized conditions. The calibration curve was created using peak area (Figure 2H), and the results showed a good level of linearity over the range of concentrations tested with a calibration curve of $Y = 4.538X - 5.791$ and $R^2 = 0.9991$. The results showed that the retention time for the peak corresponding to free SeMet in each sample was the same at 2.2 min by the validated method (Figure 2I), while the peak corresponding to SeMet-LP was not found. The specificity of the method for SeMet in these liposomal formulations was confirmed by the unchanged chromatographic behavior after encapsulation and RGD modification.

In vivo biodistribution of intravenously administered LP@RGD in mice

We assessed aortic targeting after intravenous administration of DIR-labeled LP@RGD (DIR-LP@RGD) in mouse models of AAA and TAD. *In vivo* fluorescence imaging was performed at 1, 7, 14, and 28 days after tail-vein injection. The signal declined over time but remained clearly detectable on day 28 (Figure 3A-B). *Ex vivo* imaging of harvested aortas showed selective accumulation in lesions in both models, with negligible fluorescence in unaffected segments. Compared with liposomes lacking RGD (DIR-LP), DIR-LP@RGD produced significantly stronger signals in the diseased aortic wall (Figure 3C-D).

We also imaged the heart, lung, liver, spleen, and kidney from the PBS, SeMet, SeMet-LP@RGD, and SeMet-LP groups. Strong fluorescence was detected mainly in the livers of mice receiving SeMet-LP@RGD or SeMet-LP; signals were negligible in the other organs and in the PBS and free SeMet groups. Hepatic fluorescence was markedly lower with SeMet-LP@RGD than with SeMet-LP, suggesting that RGD-mediated targeting reduced nonspecific liver accumulation and improved vascular targeting (Figure S3). To identify the cells associated with the carrier, we stained lesional aortic segments from DIR-LP@RGD-treated mice for CD68 or α-SMA. DIR-LP@RGD fluorescence overlapped extensively with $CD68^+$ macrophages and $\alpha\text{-SMA}^+$ VSMCs in both models (Figure 3E-F). These findings demonstrate selective delivery to the two cell populations within diseased aortic tissue.

RGD modification enhances nanoliposome uptake by M1 macrophages and synthetic VSMCs

To identify the macrophage subsets responsible for LP@RGD uptake, we treated RAW 264.7 cells with PBS, LPS, or IL-4 to generate M0, M1, and M2 populations, respectively. Cells were then incubated with Dil-labeled empty liposomes (Dil-LP) or RGD-functionalized liposomes (Dil-LP@RGD). Confocal imaging showed comparable Dil-LP uptake across all three populations (Figure 4A). With Dil-LP@RGD, however, fluorescence intensity was markedly higher in M1 macrophages than in M0 or M2 macrophages (Figure 4B). Flow cytometry confirmed the confocal imaging results (Figures 4C-D), demonstrating preferential recognition and uptake of RGD-functionalized liposomes by M1 macrophages. These cells are major contributors to inflammation and matrix degradation in TAD and AAA lesions.

We next compared liposome uptake in contractile and synthetic VSMCs under similar conditions. Dil-LP uptake was nearly identical in the two phenotypes (Figure 4E), whereas Dil-LP@RGD uptake was markedly higher in synthetic VSMCs (Figure 4F). Flow cytometry confirmed this preference (Figure 4G-H), showing that RGD modification confers selectivity for

synthetic VSMCs. To test whether uptake depended on RGD binding to integrin αvβ3, we blocked the receptor with c(RGDyK) peptide [13]. Receptor blockade substantially reduced LP@RGD internalization in both M1 macrophages and synthetic VSMCs relative to unblocked controls (Figure S4). Together, the uptake and blocking experiments support RGD-engineered liposomes as a targeted delivery vehicle for both cell populations in TAD and AAA.

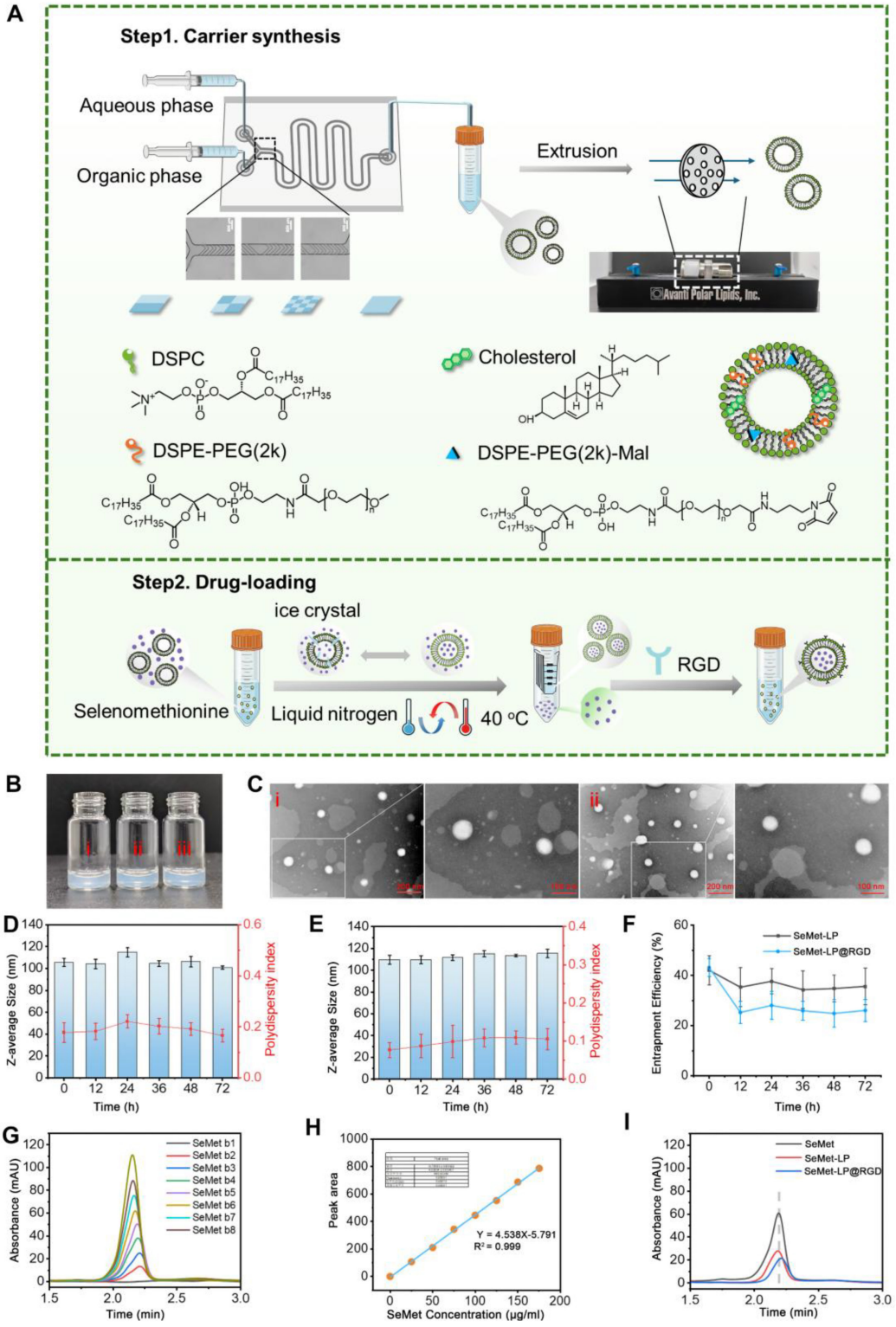


Figure 2. Design and characterization of the SeMet-LP@RGD nanodrug. (A) Schematic illustration of the fabrication process for SeMet nanomedicine. (B) Photographic images of the SeMet nanomedicine at key preparation stages: (i) blank liposomes after microfluidic mixing, (ii) liposomes after extrusion, and (iii) drug-loaded liposomes after the freeze-thaw cycle. All dispersions appear clear and homogeneous. (C) Representative transmission electron microscopy (TEM) images of (i) blank liposomes (LP) and (ii) SeMet-loaded liposomes (SeMet-LP). Scale bars: 200 nm, and 100 nm (magnified photographs). (D) Stability assessment of SeMet-LP. Hydrodynamic diameter and

polydispersity index (PDI) of SeMet-LP stored at 4°C were monitored by dynamic light scattering (DLS) over 72 hours. (E) Stability assessment of SeMet-LP@RGD. Hydrodynamic diameter and PDI of RGD-conjugated, SeMet-loaded liposomes (SeMet-LP@RGD) stored at 4°C were monitored by DLS over 72 hours. (F) Stability of drug encapsulation. The encapsulation efficiency (EE%) of both SeMet-LP and SeMet-LP@RGD formulations was measured over 72 hours of storage at 4°C. (G) Representative high-performance liquid chromatography (HPLC) chromatogram of a standard SeMet solution. (H) Standard calibration curve for SeMet quantification. The curve was generated by plotting the HPLC peak area against the known concentration of SeMet standards. (I) Representative HPLC chromatograms of the SeMet-LP and SeMet-LP@RGD formulations.

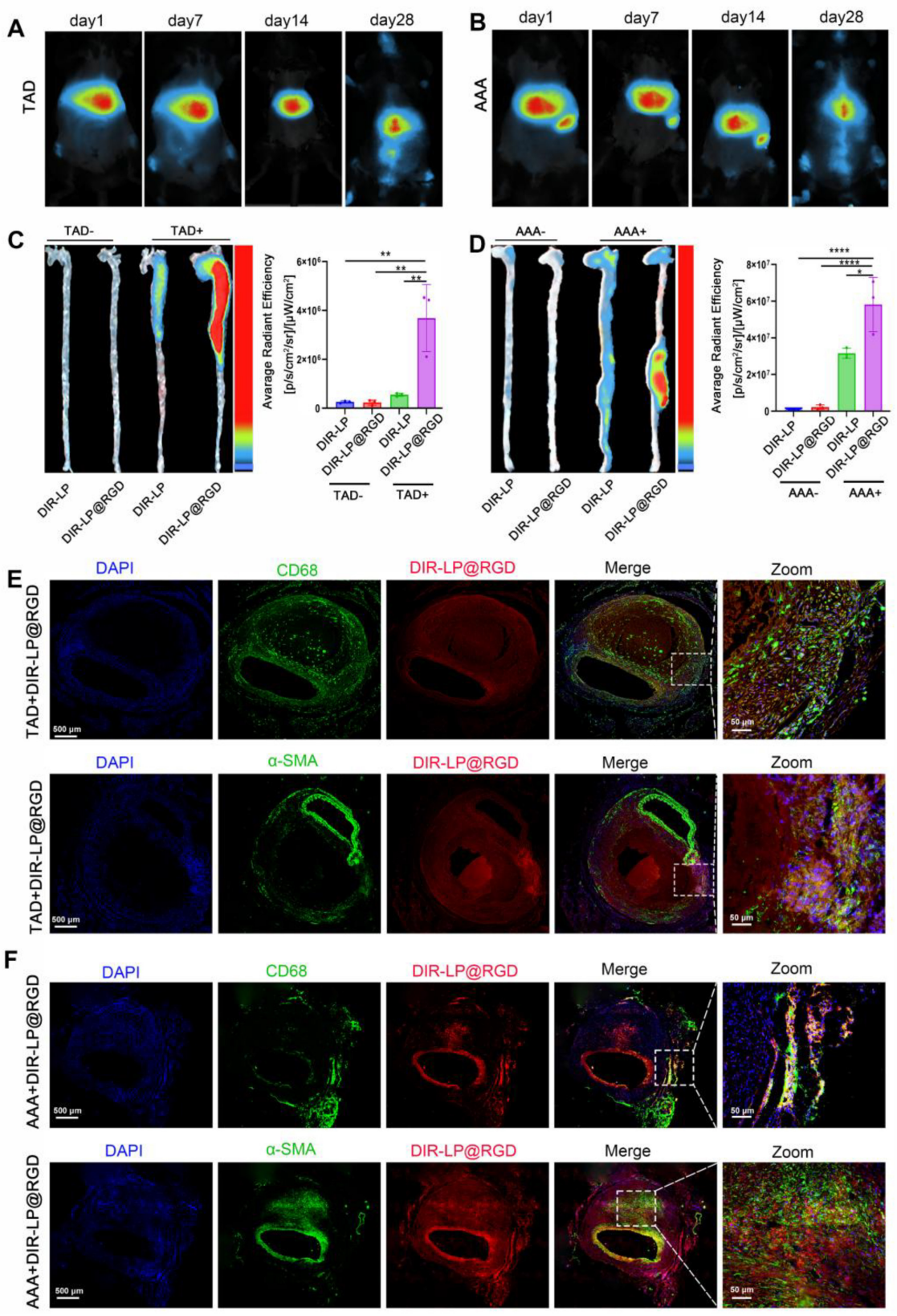


Figure 3. *In vivo* targeting capability of intravenously administered LP@RGD in both TAD and AAA mouse models. (A-B) *In vivo* imaging system (IVIS) indicate the retention effect of accumulated DIR-LP@RGD in TAD mice (A) and AAA mice (B). (C-D) Representative aortic images and fluorescence intensity analysis from the IVIS of

normal tissue or TAD (C) and AAA (D) tissues 28 days after intravenous injection. (E-F) Representative images of TAD (E) and AAA (F) sections stained with anti-CD68 antibody (macrophages) and anti-αSMA antibody (VSMCs) in TAD and AAA mice injected with DIR-LP@RGD(scale bars: 500 μm, 50 μm).

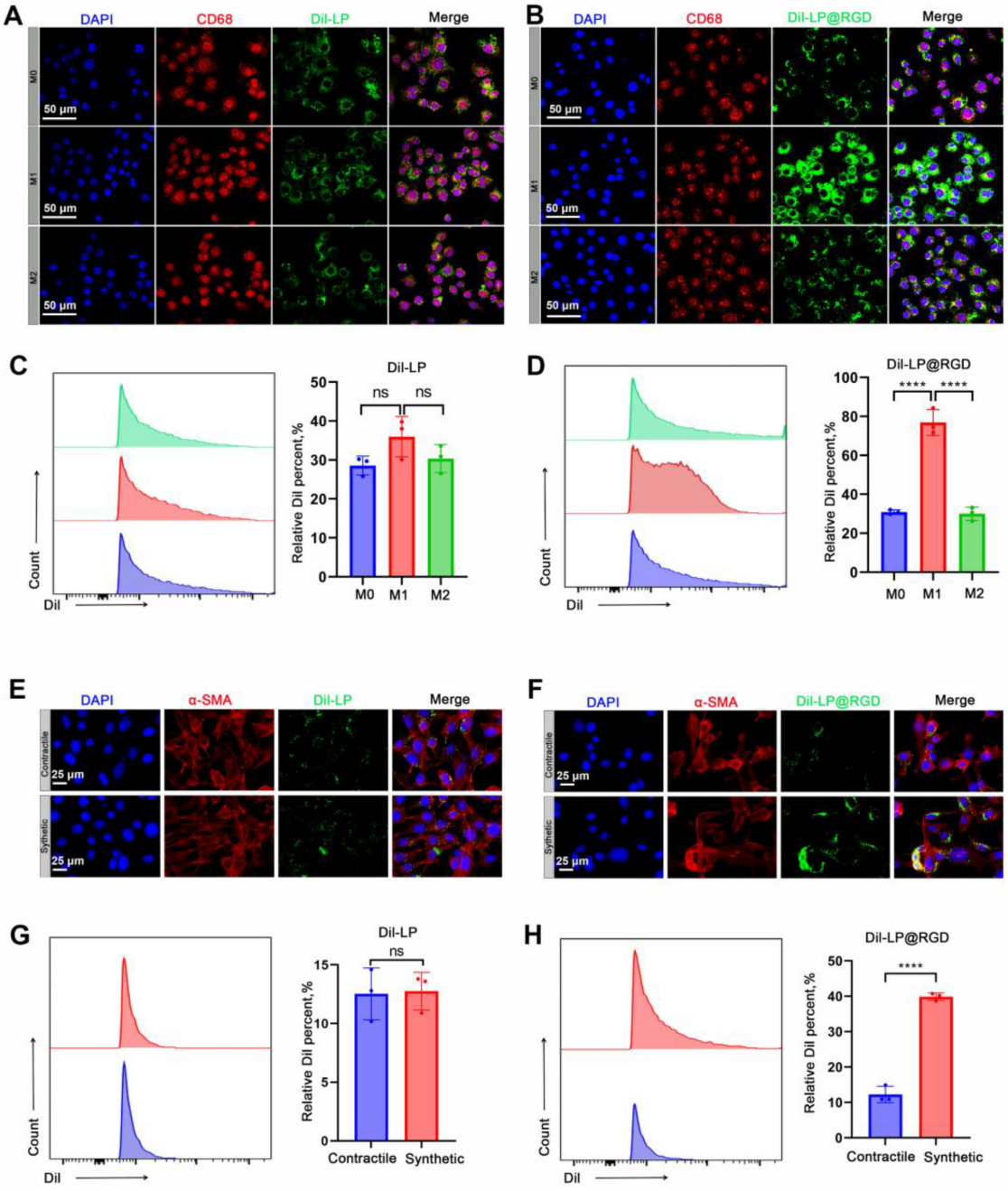


Figure 4. RGD modification enhances nanoliposome uptake by M1 macrophages and synthetic VSMCs. (A-B) Confocal laser scanning microscope (CLSM) images showing the cellular uptake of Dil-LP (A) and Dil-LP@RGD (B) by M0, M1, and M2 macrophages *in vitro*. Scale bars, 50 μm. (C-D) Flow cytometry profiles and quantitative analysis of Dil-LP (C) and Dil-LP@RGD (D) uptake in M0, M1, and M2 macrophages (n=3). (E-F) CLSM images illustrating the cellular internalization of Dil-LP (E) and Dil-LP@RGD (F) by contractile and synthetic VSMCs. Scale bars, 50 μm. (G-H) Flow cytometric profiles and quantitative analysis of Dil-LP (G) and Dil-LP@RGD (H) uptake in contractile and synthetic VSMCs (n=3).

SeMet-LP@RGD ameliorates BAPN-induced TAD formation in mice

We evaluated SeMet-LP@RGD in mice with BAPN-induced TAD. Mice were randomly assigned to untreated Control, BAPN+Saline, BAPN+SeMet, BAPN+SeMet-LP, or BAPN+SeMet-LP@RGD groups; SeMet-LP@RGD was administered through the tail vein. Aortas were harvested 28 days after treatment (Figure 5A). Spontaneous aortic rupture caused death in 75% of the BAPN+Saline group. Mortality was lower in all treatment groups and lowest with SeMet-LP@RGD at 35%. The SeMet-LP@RGD group also had the lowest TAD incidence, at 60% (Figure 5B). Maximum lesion diameter was substantially greater in BAPN+Saline mice than in normal controls,

confirming TAD model induction. SeMet, SeMet-LP, and SeMet-LP@RGD all reduced aortic dilation relative to BAPN+Saline, with greater protection from SeMet-LP@RGD than from untargeted SeMet-LP (Figure 5C). H&E and elastic van-Gieson (EVG) staining showed that SeMet-LP@RGD reduced vessel wall injury and preserved the continuity of elastic lamellae (Figure 5D-G), supporting its protective effect against TAD progression. Immunofluorescence staining revealed extensive $CD86^+$ M1 macrophage infiltration in the diseased thoracic aorta of BAPN+Saline mice. Free SeMet and both liposomal formulations shifted polarization toward $CD206^+$ M2 macrophages, with the largest shift in the SeMet-LP@RGD group (Figure 5E). Western blotting likewise showed significantly lower inducible nitric oxide synthase (iNOS) expression and markedly higher arginase-1 (Arg1) expression after SeMet-LP@RGD treatment, with stronger effects than those of SeMet or SeMet-LP (Figure 5H). These results indicate a shift toward an anti-inflammatory M2 phenotype.

TUNEL staining showed a significantly lower rate of VSMC apoptosis in lesional aortas after SeMet-LP@RGD treatment than after saline treatment; the reduction was also greater than with SeMet or SeMet-LP (Figure 5F). SeMet-LP@RGD produced the strongest reversal of BAPN-induced VSMC phenotypic switching, restoring the contractile markers α-smooth muscle actin (α-SMA) and smooth muscle myosin heavy chain (SM-MHC) while suppressing the synthetic markers vimentin and osteopontin (OPN) (Figure 5I). This preservation of contractile marker expression accompanied the reduced apoptosis and vessel wall injury.

In a separate biosafety assessment, mice were randomly assigned to normal saline, SeMet, or SeMet-LP@RGD treatment. After 28 days, the heart, liver, spleen, lung, and kidney were examined by H&E staining, and serum creatinine (CREA), blood urea nitrogen (BUN), alanine aminotransferase (ALT), and aspartate aminotransferase (AST) were measured. No significant differences in tissue histology or these serum markers were detected among the three groups, supporting favorable biosafety under the tested conditions (Figure S5).

SeMet-LP@RGD attenuates AngII-induced AAA formation in mice

After observing improved survival and reduced pathological progression in TAD mice, we evaluated SeMet-LP@RGD in an AAA model using $ApoE^{-/-}$ mice. Animals were randomly assigned to 5 groups: Control, AngII+Saline, AngII+SeMet, AngII+SeMet-LP, and AngII+SeMet-LP@RGD. Representative aortas are shown in Figure 6A. AAA incidence was 73% with AngII+Saline, 47% with SeMet, and 40% with SeMet-LP, and was lowest with SeMet-LP@RGD at 20% (Figure 6B). Measurements of maximum lesion diameter showed substantial abdominal aortic dilation after AngII infusion. Both free SeMet and SeMet-LP attenuated this dilation. SeMet-LP@RGD reduced aortic enlargement more than untargeted SeMet-LP (Figure 6C). H&E staining showed better preservation of aortic wall structure, and EVG staining showed less elastin degradation in the SeMet-LP@RGD group (Figure 6D-G).

We then examined macrophage polarization within the lesions. $CD86^+$ M1-like macrophages predominated in AngII-induced AAA, whereas treatment with free SeMet, SeMet-LP, or SeMet-LP@RGD shifted polarization toward the $CD206^+$ M2-like phenotype. The shift was greatest with SeMet-LP@RGD (Figure 6E). Consistent with these findings, SeMet-LP@RGD significantly reduced iNOS expression and increased Arg1 expression, indicating a shift toward an anti-inflammatory aortic microenvironment (Figure 6H). TUNEL staining showed a significantly lower proportion of apoptotic cells with SeMet-LP@RGD than in the other groups (Figure 6F). Western blotting further showed reversal of the AngII-induced decrease in α-SMA and SM-MHC and increase in vimentin and OPN (Figure 6I). These findings support preservation of the VSMC contractile phenotype alongside reduced apoptosis and inflammation.

SeMet-LP@RGD modulates macrophage polarization via suppression of the NF-κB signaling pathway

We next examined macrophage polarization *in vitro*. Compared with the PBS control, SeMet, SeMet-LP, and SeMet-LP@RGD significantly reduced iNOS protein expression and increased Arg1 expression. SeMet-LP@RGD produced the strongest, statistically significant response among the tested groups (Figure 7A). Immunofluorescence imaging showed more Arg1-expressing cells and fewer iNOS-positive cells after SeMet-LP@RGD treatment, indicating a shift toward the M2-like phenotype (Figure 7B). ELISA measurements showed that free SeMet and untargeted SeMet-LP reduced IL-1β and IL-6 secretion while increasing IL-10 and TGF-β production. SeMet-LP@RGD had stronger effects than SeMet-LP on all four cytokines (Figure 7C). Our earlier laboratory research reported that SeMet modulates NF-κB signaling, a key regulator of macrophage polarization and inflammation [17]. We therefore tested whether SeMet-LP@RGD altered activation of this pathway. RAW 264.7 macrophages were pre-incubated with SeMet-LP@RGD or vehicle before LPS stimulation to

induce M1-dominant polarization. LPS markedly increased phosphorylation of IKKα, IκBα, and NF-κB. Pre-incubation with SeMet-LP@RGD substantially blunted these increases relative to LPS alone (Figure 7D). Suppression of the IKKα/IκBα/NF-κB pathway was also observed in the AngII-induced AAA model (Figure S6). These findings indicate that SeMet-LP@RGD inhibits the IKKα/IκBα/NF-κB axis to attenuate inflammatory activation and favor a shift from M1 to M2 polarization.

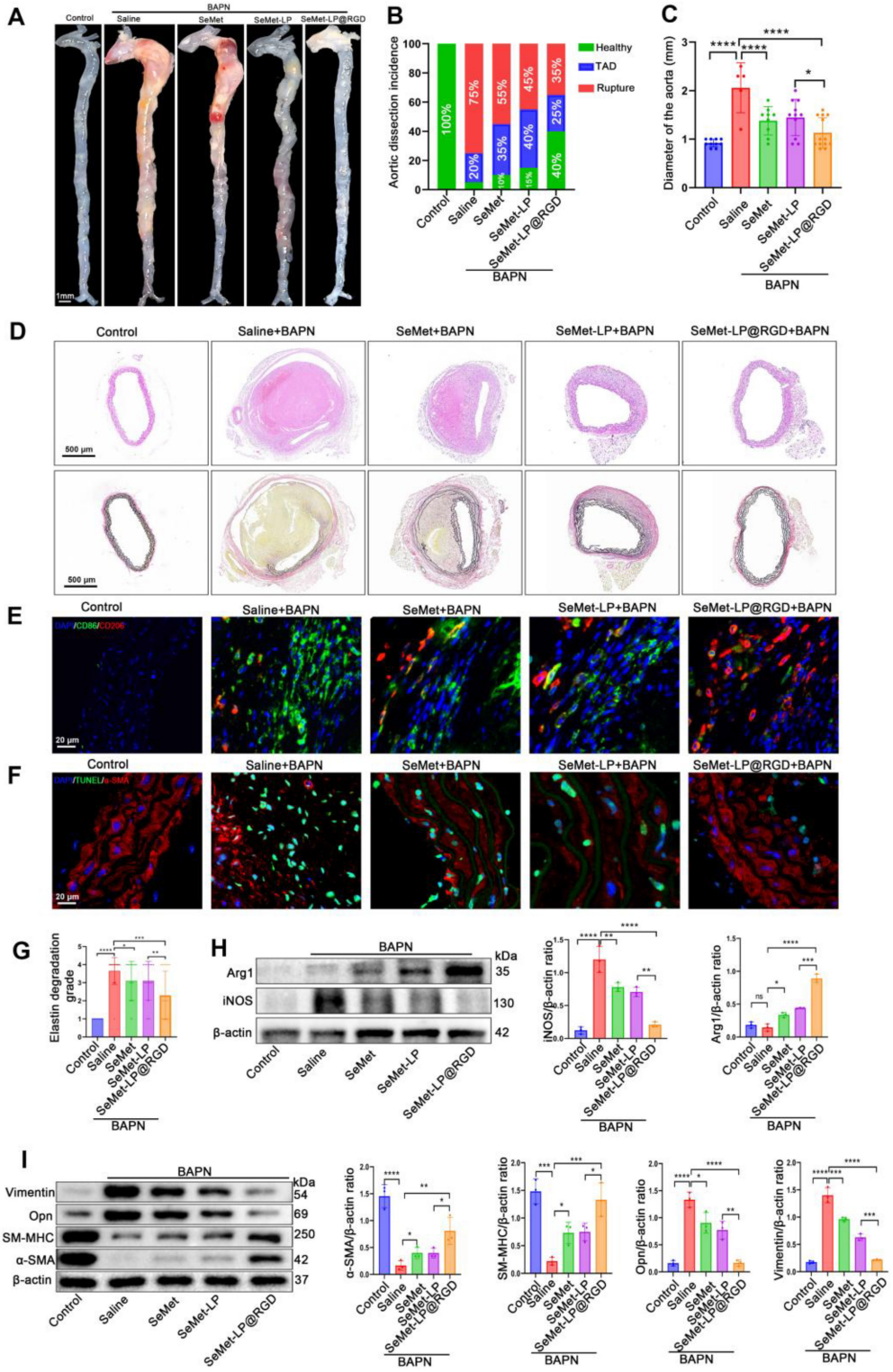


Figure 5. Evaluation of SeMet-LP@RGD therapeutic efficacy in a mouse model of TAD. (A) Representative macroscopic images of aortas from mice treated with Control, BAPN+Saline, BAPN+SeMet, BAPN+SeMet-LP, or BAPN+SeMet-LP@RGD.Scale bar: 1 mm. (B) Incidence of aortic dissection in mice across treatment groups. (C) Quantification of the TAD maximum aortic diameters (Control n=10, The other group n=20). (D) Histological analysis using H&E and EVG staining. Scale bars: 500 μm. (E) Immunofluorescence staining for M1-like ($CD86^+$) and M2-like ($CD206^+$) macrophages. Scale bars: 20 μm. (F) TUNEL assay for detection of apoptotic VSMCs. Scale bars: 20

μm. (G) The elastin degradation score of aortas from mice treated with Control, BAPN+Saline, BAPN+SeMet, BAPN+SeMet-LP, or BAPN+SeMet-LP@RGD. (H) Western blot analysis and quantification of iNOS and Arg-1 expression in aortic tissues (n=3). (I) Western blot analysis and quantification of contractile (αSMA, SM-MHC) and synthetic (OPN, Vimentin) phenotypic markers in aortic tissues (n=3).

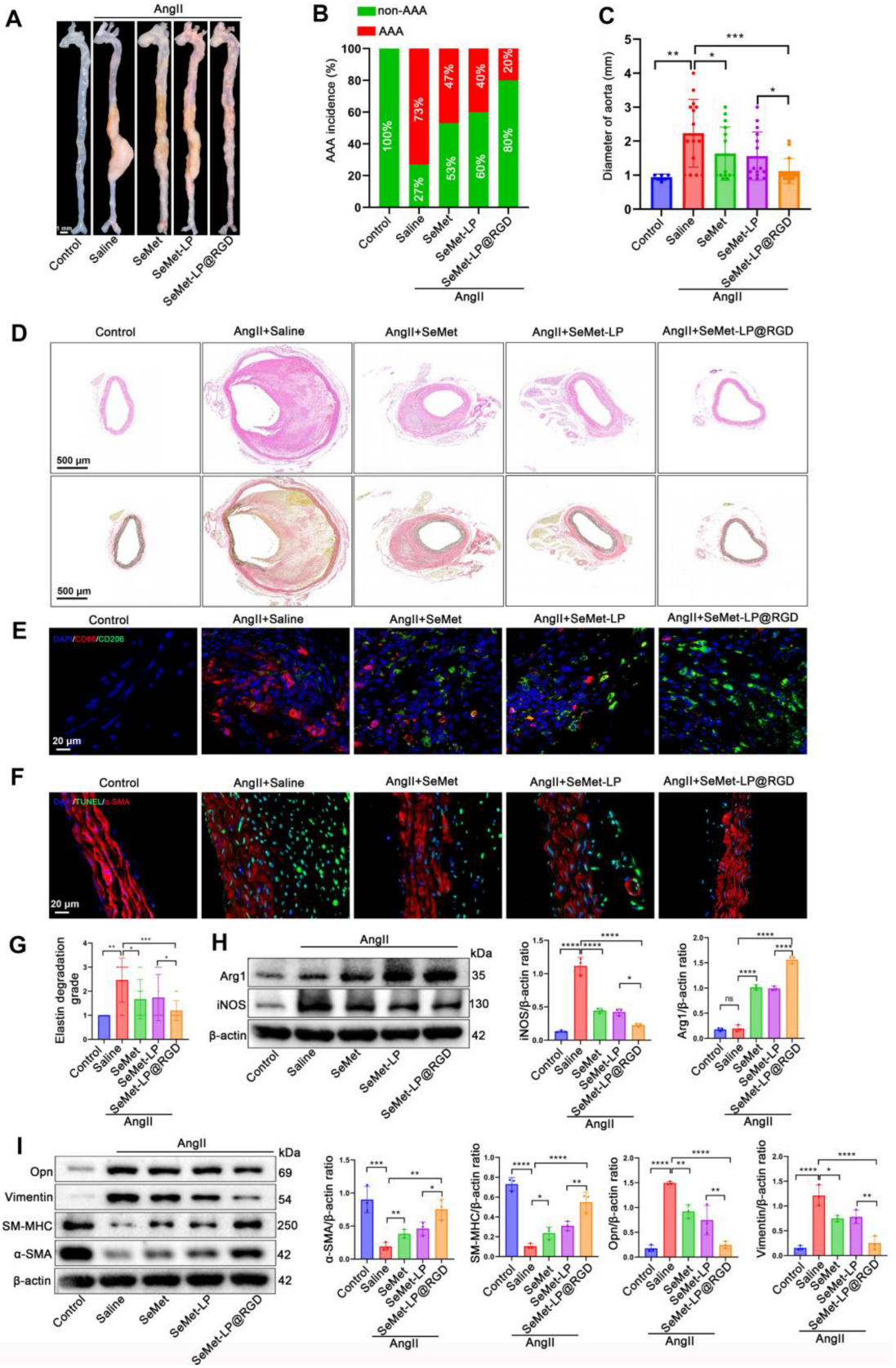


Figure 6. Evaluation of SeMet-LP@RGD therapeutic efficacy in a mouse model of AAA. (A) Representative macroscopic images of aortas from mice treated with Control, AngII+Saline, AngII+SeMet, AngII+SeMet-LP, or AngII+SeMet-LP@RGD. Scale bar: 1 mm. (B) Incidence of AAA in mice across treatment groups (Control n=5, The

other group n=15). (C) Quantification of maximum abdominal aortic diameters. (D) Histological analysis via H&E and EVG staining. Scale bars: 500 μm. (E) Immunofluorescence staining for M1-like (CD86$^+$) and M2-like (CD206$^+$) macrophages. Scale bars: 20 μm. (F) TUNEL assay detecting apoptotic VSMCs. Scale bars: 20 μm. (G) The elastin degradation score of aortas from mice treated with Control, AngII+Saline, AngII+SeMet, AngII+SeMet-LP, or AngII+SeMet-LP@RGD. (H) Western blot analysis and quantification of iNOS and Arg-1 expression in aortic tissues (n=3). (I) Western blot analysis and quantification of contractile (αSMA, SM-MHC) and synthetic (OPN, Vimentin) phenotypic markers in aortic tissues (n=3).

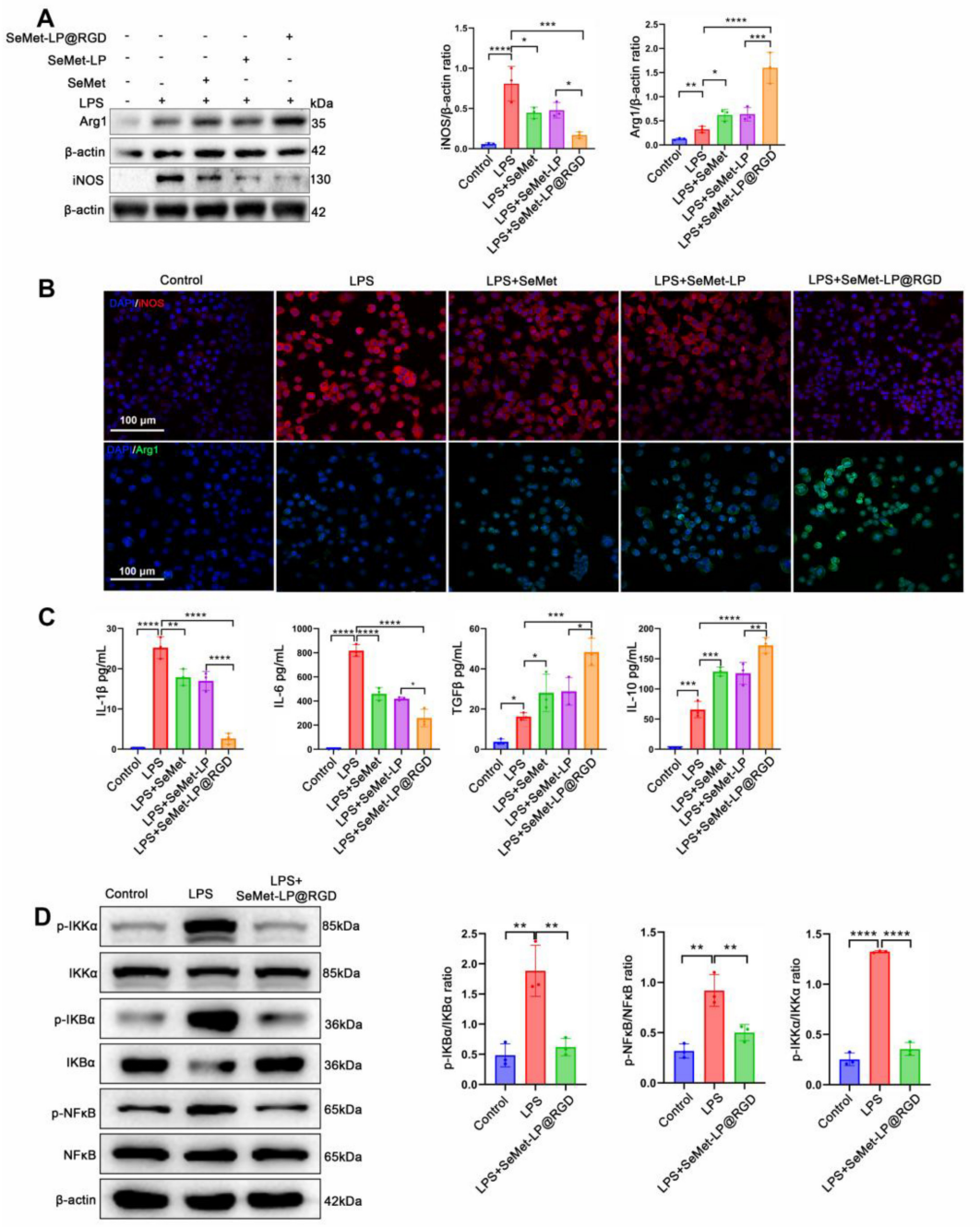


Figure 7. SeMet-LP@RGD modulates macrophage polarization via the NF-κB signaling pathway. (A) Representative images of western blots and statistical analysis for protein levels of iNOS (M1) and Arg1 (M2) expression in LPS-stimulated RAW264.7 macrophages treated with SeMet, SeMet-LP, or SeMet-LP@RGD (n=3). (B) Immunofluorescence staining depicting M1 (iNOS$^+$) and M2 (Arg1$^+$) macrophage subtypes per group. Scale bars, 100 μm. (C) Cytokine levels measured in cell culture supernatant, including the pro-inflammatory factors IL-1βand IL-6, and the anti-inflammatory factors IL-10 and TGF-β per group (n=3). (D) Representative images of western blots and statistical analysis for protein levels of IκKα, p-IκKα, IκBα, p-IκBα, NF-κB, and p-NF-κB in the cells of the control, LPS and LPS + SeMet-LP@RGD groups (n=3).

Integrated multi-omics analysis shows that SeMet-LP@RGD suppresses pathological VSMC phenotypic switching by inhibiting BRD4 lactylation

We examined the effects of SeMet-LP@RGD on VSMCs because their dysfunction is central to TAD and AAA. AngII stimulation significantly decreased α-SMA and SM-MHC expression and increased vimentin and OPN expression, confirming a shift

toward the synthetic phenotype. SeMet, SeMet-LP, and SeMet-LP@RGD partially reversed these changes, with SeMet-LP@RGD producing the greatest recovery of contractile markers and suppression of synthetic markers (Figure 8A). To assess an indirect effect mediated by macrophage-derived factors, we collected supernatants from RAW264.7 cells under control, LPS, and LPS+SeMet-LP@RGD conditions and applied them to VSMCs. Supernatant from the LPS+SeMet-LP@RGD group reversed the LPS-triggered phenotypic changes (Figure S7). These results indicate that SeMet-LP@RGD acts directly on VSMCs and indirectly through changes in macrophage polarization and inflammatory signaling.

We then used quantitative metabolomics and KEGG enrichment analysis to investigate the underlying mechanism. Treatment altered the VSMC energy metabolism profile, and differentially abundant metabolites were significantly enriched in the glycolytic pathway (Figure 8B), suggesting a metabolic contribution to phenotype regulation. Because glycolysis is the main source of intracellular lactate, we measured lactate in culture supernatants from the Control, AngII, and AngII+SeMet-LP@RGD groups. SeMet-LP@RGD significantly reduced AngII-induced lactate production (Figure 8C). We next examined global lactylation (Pan-Kla) in Control, SeMet-LP@RGD, AngII, and AngII+SeMet-LP@RGD VSMCs. AngII significantly increased Pan-Kla levels; SeMet-LP@RGD markedly suppressed this increase and restored levels close to baseline (Figure 8D). After quality control, we performed principal component analysis (PCA) on the proteomic and lactylomic datasets from the AngII and AngII+SeMet-LP@RGD groups (Figure 8E-F). We intersected the 8,377 proteins with unchanged abundance in the proteomic analysis with the 33 proteins showing significantly reduced lactylation after treatment. This identified 32 proteins with decreased lactylation but stable total abundance (Figure 8G), whose lactylation profiles are shown in Figure 8H. BRD4 was among these candidates. This BET-family epigenetic regulator drives abnormal VSMC activation after AngII stimulation. Our data suggest that SeMet-LP@RGD limits BRD4 transcriptional co-activator activity by reducing its lactylation without changing total protein abundance, thereby restraining the synthetic transition.

We combined sequence-motif prediction, site-specific lactylation quantification, and LC-MS/MS to identify the responsive lysine residues. Treatment significantly reduced lactylation at BRD4 residues 696 and 1234 (K696 and K1234) (Figure 8I-J). The sites had distinct conserved motifs: K696 contained an S-K core motif (Figure 8K), whereas the K1234 motif contained conserved lysines at the second and seventh positions (Figure 8L). These differences suggest recognition by different modifying enzymes with distinct sequence preferences. LC-MS/MS spectra contained abundant b/y fragment ions identifying peptides with K696 and K1234, confirming both modification sites (Figure 8M-N). We therefore propose that inhibition of pathological BRD4 lactylation contributes to preserved VSMC contractility and may limit BRD4-dependent transcriptional reprogramming during phenotypic switching.

SeMet-LP@RGD regulates VSMC phenotypic switching through BRD4 lactylation at K1234

Having identified BRD4 lactylation at K696 and K1234, we investigated which site mediates VSMC phenotypic switching and the response to SeMet-LP@RGD. Co-immunoprecipitation (Co-IP) and western blotting showed that increasing sodium lactate concentrations produced a dose-dependent increase in the Pan-Lactyllysine (Pan-Kla) signal on BRD4 in VSMCs (Figure 9A), confirming the lactylation detected by proteomics. AngII significantly increased BRD4 lactylation, whereas SeMet-LP@RGD significantly inhibited this response (Figure 9B). The same pattern was observed in the AngII-induced AAA model (Figure S8). We then generated K696R and K1234R mutants, substituting arginine for lysine to block lactylation, and assessed them by Co-IP and western blotting. AngII significantly increased BRD4 lactylation in cells expressing wild-type (WT) BRD4. The K696R mutation did not affect this response, whereas K1234R completely abolished AngII-induced lactylation (Figure 9C). SeMet-LP@RGD significantly reduced lactylation in cells expressing WT BRD4 or K696R, but caused no significant change in K1234R-expressing cells (Figure 9D). Thus, K1234 is the necessary, selective functional site for the lactylation response to AngII and its inhibition by SeMet-LP@RGD; K696 made no significant functional contribution in this pathway.

In rescue experiments, the K1234T mutant was used to mimic constitutive lactylation, based on the similar spatial conformation of threonine and lactylated lysine. K1234T expression completely counteracted the effect of SeMet-LP@RGD on AngII-induced phenotypic switching: treatment no longer reduced OPN and vimentin or increased SM-MHC and α-SMA (Figure 9E). These experiments identify K1234 lactylation as a molecular switch linking AngII signaling to VSMC phenotypic instability and as the site through which SeMet-LP@RGD exerts its phenotypic regulatory effect.

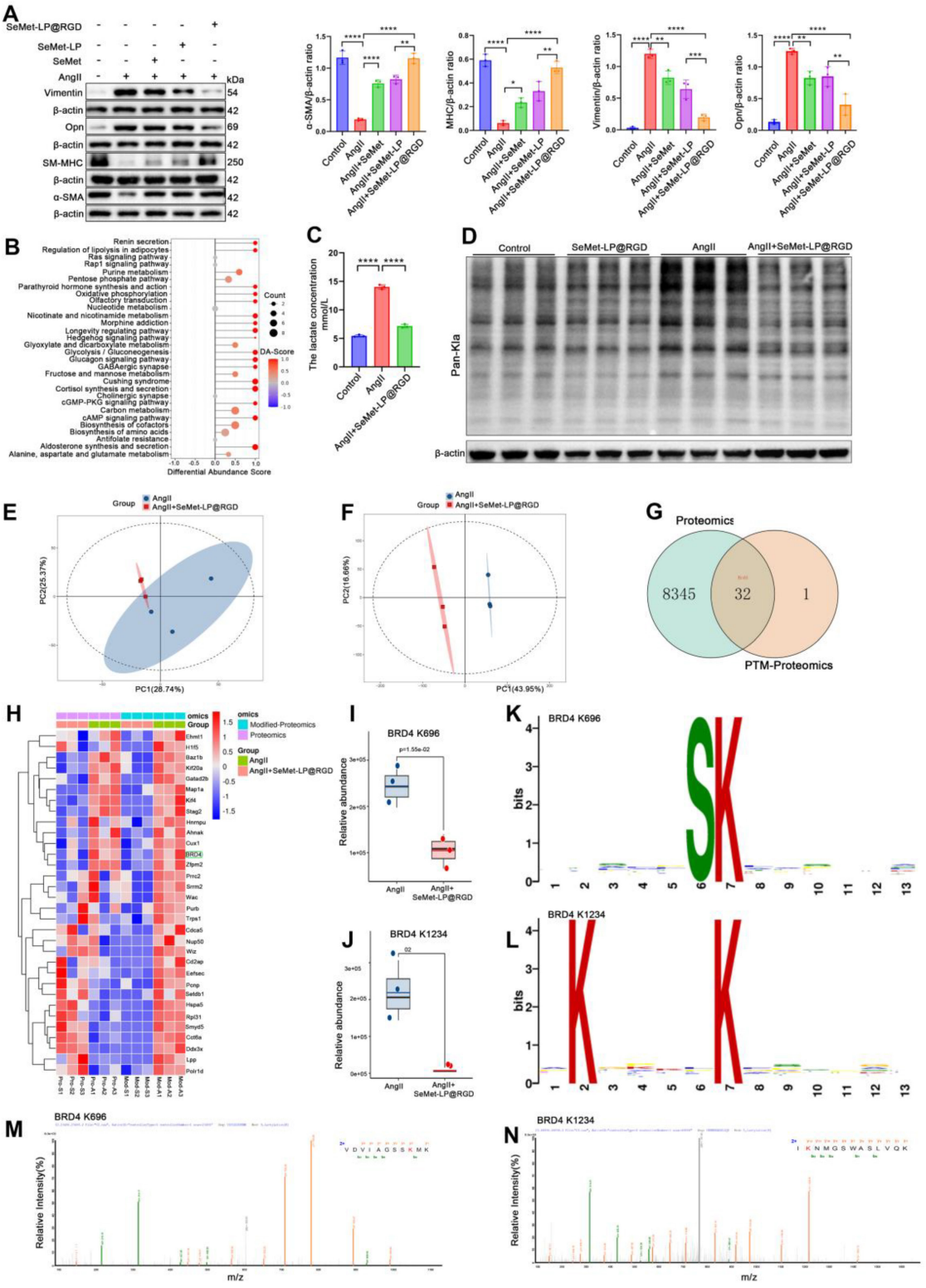


Figure 8. Multi-omics analysis reveals that SeMet-LP@RGD mediates VSMC phenotypic switching by regulating BRD4 lactylation. (A) Representative images of western blots and statistical analysis for protein levels of the contractile markers αSMA and SM-MHC, and the synthetic markers Vimentin and OPN (n=3). (B) Differential Abundance Score(DA Score) plot of enriched KEGG pathways. DA Score (x-axis) indicates the enrichment direction and magnitude, with pathway names listed on the y-axis. Dot color represents DA Score (red=upregulation, blue=downregulation) and dot size denotes the number of differentially abundant molecules in each pathway. (C) Quantitative measurement of lactate concentration from samples of Control, AngII, and AngII+SeMet-LP@RGD groups (n=3). (D) Western blot analysis of global lysine lactylation (Pan-Kla) in Control, SeMet-LP@RGD, AngII, and AngII+SeMet-LP@RGD treated VSMCs. β-actin served as the loading control. (E, F) Principal Component Analysis (PCA) of proteomic (E) and PTM-proteomic (F) data. (G) Venn diagram showing the overlap between global proteomics and PTM-proteomics datasets. A total of 32 proteins, including Brd4, were commonly identified in both analyses, with 8345 proteins unique to global proteomics and 1 protein unique to PTM-proteomics. (H) The cluster heatmap depicting the 32 target proteins exhibiting significantly downregulated lactylation levels alongside stable protein expression. (I, J) Boxplots of BRD4 lactylation abundance at K696 (I) and K1234 (J) residues. (K, L) Sequence logos of the BRD4 lactylation sites K696 (K) and K1234 (L). (M, N) Representative LC-MS/MS analysis confirming lactylation at BRD4 lysine residues K696 (M) and K1234 (N), identifying BRD4 as a key lactylation target.

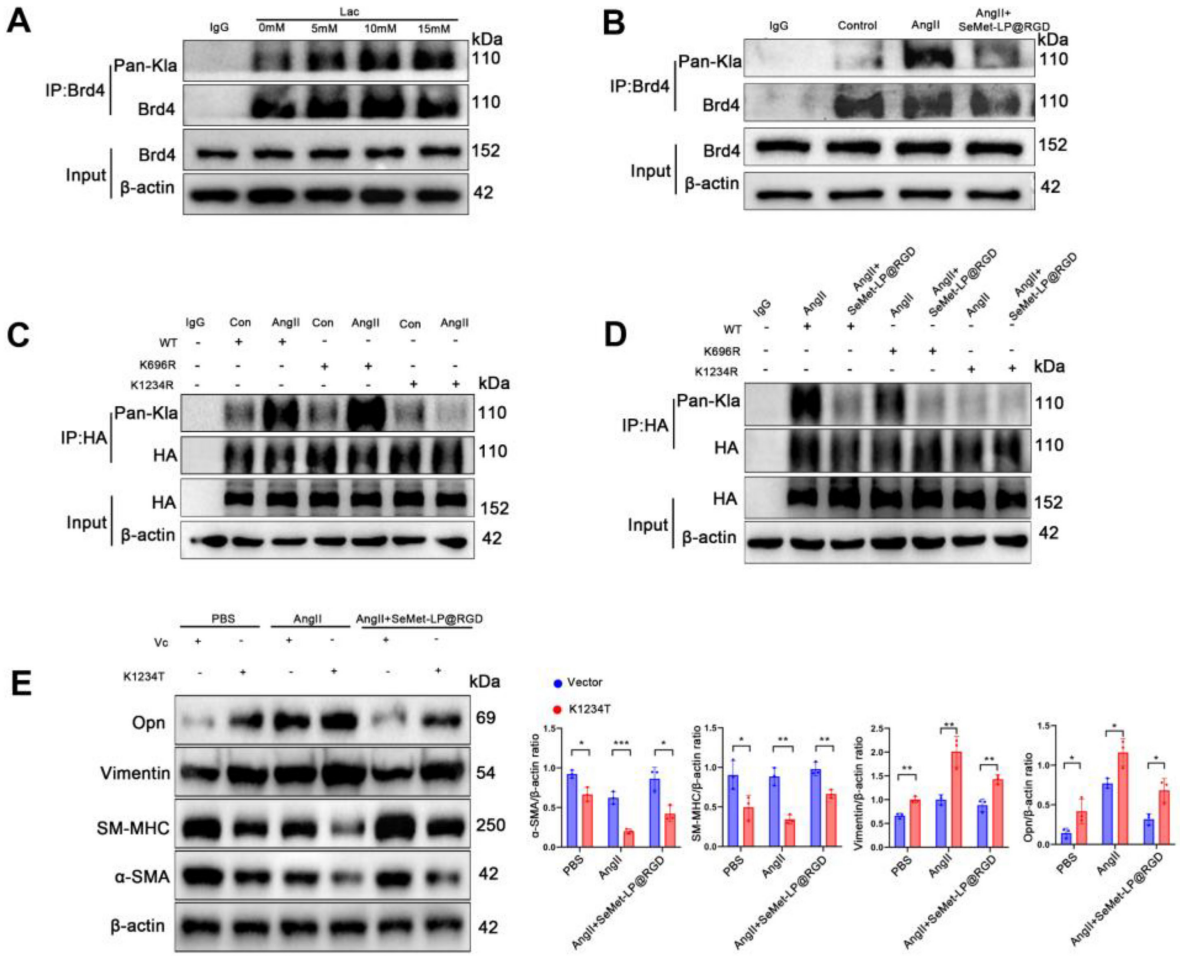


Figure 9. SeMet-LP@RGD mediates VSMC phenotypic switching by regulating BRD4 lactylation at lysine residue K1234. (A) *In vitro* lactylation assay assessing BRD4 lactylation levels in VSMCs exposed to escalating concentrations of sodium lactate (0, 5, 10, or 15 mM). (B) Co-immunoprecipitation (Co-IP) analysis of Pan-Kla on BRD4 in VSMCs following treatment with control, AngII, or AngII+SeMet-LP@RGD. IgG served as the negative control, and β-actin was used as a loading control. (C) Co-IP analysis of BRD4 lactylation in VSMCs transfected with wild-type (WT) BRD4 or lysine-to-arginine (K→R) substitution mutants at K696 or K1234, under control or AngII-stimulated conditions. (D) IP-western blot analysis of BRD4 lactylation. VSMCs were transfected with WT, K696R, or K1234R BRD4 constructs and treated with AngII±SeMet-LP@RGD. HA-tagged BRD4 was immunoprecipitated, and lactylation was detected with a Pan-Kla antibody. (E) Western blot analysis and quantitative validation of VSMC phenotypic marker expression in cells transfected with empty vector or BRD4 K1234T mutant, treated with PBS, AngII, or AngII + SeMet-LP@RGD (n=3).

Discussion

No pharmacological treatment has yet been proven to prevent aortic aneurysm progression or rupture despite extensive clinical investigation [1]. We developed and characterized SeMet-LP@RGD to address this gap by delivering SeMet to both pro-inflammatory M1 macrophages and synthetic VSMCs, and evaluated its therapeutic effects in models of aortic aneurysm and dissection. Cell culture and mouse experiments confirmed preferential targeting of integrin αvβ3-rich M1 macrophages and synthetic VSMCs by RGD-modified liposomes. In the mouse models, SeMet-LP@RGD reduced aortic expansion and lethal dissection and preserved vessel wall integrity more effectively than free SeMet or untargeted liposomes. The mechanistic findings linked this protection to suppression of excessive NF-κB signaling in macrophages and inhibition of BRD4 K1234 lactylation in VSMCs. These effects reduced local inflammation while maintaining the VSMC contractile phenotype.

RGD-mediated recognition of integrin αvβ3 allows the same carrier to reach both cell populations. Many nanomedicines developed for AAD have focused on macrophages alone [18, 19]. Here, uptake assays showed efficient internalization by M1 macrophages and synthetic VSMCs, and *in vivo* imaging localized the carrier to both populations in aortic lesions. Macrophage repolarization reduces the inflammatory burden, while direct effects on VSMCs preserve vessel wall integrity. Their combined action provides a basis for synergistic treatment effects and may explain the efficacy observed in our animal models. Targeting both populations therefore offers a

functional advantage over approaches directed at a single cell type.

These findings are consistent with the roles of inflammation and oxidative stress in AAD progression [20, 21]. RGD-mediated vascular targeting has been investigated in atherosclerosis models [22], but its use to target both M1 macrophages and synthetic VSMCs for AAD treatment has not previously been reported. Antioxidant-loaded nanocarriers have also been described [23]. Our formulation combines the dual activity of SeMet with integrin-directed liposomal delivery. Its greater efficacy relative to untargeted liposomes confirms that the treatment benefit derives primarily from RGD-dependent active targeting rather than nonspecific passive accumulation.

Several limitations remain. Although widely used in AAA research, the AngII infusion model does not reproduce the slow disease course in patients. The findings therefore require validation in other animal models and in human tissues cultured *ex vivo*. Clinical translation will also require characterization of long-term SeMet-LP@RGD distribution, selenium accumulation in nontarget organs, and chronic toxicity. Further studies should establish treatment windows for prevention or reversal of disease and assess combination therapies. Controls using blank liposomes, unconjugated RGD peptide, scrambled peptide-modified liposomes, and free SeMet co-administered with soluble RGD would help distinguish the contributions of individual components to uptake, macrophage polarization, VSMC phenotypic switching, BRD4 lactylation, and NF-κB activity. Positive-control groups were also absent, including doxycycline and statins, which represent established AAA therapeutic options. Follow-up studies will include these reference groups to compare the relative potency of SeMet-LP@RGD more accurately.

Conclusion

We developed SeMet-LP@RGD to deliver selenomethionine selectively to M1-like macrophages and synthetic VSMCs in aortic aneurysm and dissection lesions. Treatment reduced local inflammation, restored immune homeostasis, and maintained the VSMC contractile phenotype. The combination of lesion-directed delivery and defined molecular effects supports further development of this formulation as a therapeutic approach for AAD.

Supplementary Material

Supplementary methods and figures.
https://www.thno.org/v17p0573s1.pdf

Acknowledgements

Funding

This work was supported by the Natural Science Foundation of China (grant numbers: 82400566, 82160072, 82374262), the Youth Project of the Natural Science Foundation of Hubei Province (2023AFB127), and Enshi Prefecture Science and Technology Bureau, selenium citation special (D20230072).

Availability of data and materials

The corresponding author will make available the data supporting the findings of this study upon reasonable request.

Author contributions

Jiamin Xu and Xi Tan: Investigation, Formal analysis, Validation, Visualization, Writing-original draft, Writing-review & editing; Ke Hu and Xu Zhou: Investigation, Writing-original draft; Lihua Tian, Xiaohan Fan, Heng Wu, Zhongnan Xia, Changzhao Liu: Investigation, Validation; Ya Wang, Xuemei Zhang, Hongbo Chen: Validation; LiXing Wu and Yuhua Lei: Conceptualization, Funding acquisition, Supervision; Jing Zhang: Funding acquisition, Methodology, Supervision, Writing - original draft; Jiaxin Hu: Conceptualization, Funding acquisition, Methodology, Project administration, Supervision, Writing - review & editing.

No artificial intelligence (AI) tools were employed for manuscript preparation, image generation, data collection or data analysis in this work. All manuscript content, figures and supporting information were produced by the authors, who bear full responsibility for the accuracy and integrity of all results and descriptions.

Ethics approval and consent to participate

All animal experiments were conducted in accordance with protocols approved by the Animal Ethics Committee of the Central Hospital of Enshi Prefecture (License number: W202507001).

Competing Interests

The authors have declared that no competing interest exists.

References

1. Golledge J, Thanigaimani S, Powell JT, Tsao PS. Pathogenesis and management of abdominal aortic aneurysm. Eur Heart J. 2023; 44: 2682-97.
2. Carrel T, Sundt TM, 3rd, von Kodolitsch Y, Czerny M. Acute aortic dissection. Lancet. 2023; 401: 773-88.
3. Schanzer A, Oderich GS. Management of Abdominal Aortic Aneurysms. N Engl J Med. 2021; 385: 1690-8.
4. Thompson RW. Detection and management of small aortic aneurysms. N Engl J Med. 2002; 346: 1484-6.

5. Klink A, Hyafil F, Rudd J, Faries P, Fuster V, Mallat Z, et al. Diagnostic and therapeutic strategies for small abdominal aortic aneurysms. Nat Rev Cardiol. 2011; 8: 338-47.
6. Golledge J, Moxon JV, Singh TP, Bown MJ, Mani K, Wanhainen A. Lack of an effective drug therapy for abdominal aortic aneurysm. J Intern Med. 2020; 288: 6-22.
7. Hu J, Li Y, Wei Z, Chen H, Sun X, Zhou Q, et al. A reduction in the vascular smooth muscle cell focal adhesion component syndecan-4 is associated with abdominal aortic aneurysm formation. Clin Transl Med. 2021; 11: e605.
8. Lin W, Hu K, Li C, Pu W, Yan X, Chen H, et al. A Multi-Bioactive Nanomicelle-Based "One Stone for Multiple Birds" Strategy for Precision Therapy of Abdominal Aortic Aneurysms. Adv Mater. 2022; 34: e2204455.
9. Raffort J, Lareyre F, Clement M, Hassen-Khodja R, Chinetti G, Mallat Z. Monocytes and macrophages in abdominal aortic aneurysm. Nat Rev Cardiol. 2017; 14: 457-71.
10. Chou E, Pirruccello JP, Ellinor PT, Lindsay ME. Genetics and mechanisms of thoracic aortic disease. Nat Rev Cardiol. 2023; 20: 168-80.
11. Gao J, Cao H, Hu G, Wu Y, Xu Y, Cui H, et al. The mechanism and therapy of aortic aneurysms. Signal Transduct Target Ther. 2023; 8: 55.
12. Rombouts KB, van Merrienboer TAR, Ket JCF, Bogunovic N, van der Velden J, Yeung KK. The role of vascular smooth muscle cells in the development of aortic aneurysms and dissections. Eur J Clin Invest. 2022; 52: e13697.
13. Mo F, Wang C, Li S, Li Z, Xiao C, Zhang Y, et al. A Dual-Targeting, Multi-Faceted Biocompatible Nanodrug Optimizes the Microenvironment to Ameliorate Abdominal Aortic Aneurysm. Adv Mater. 2024; 36: e2405761.
14. Hariharan S, Dharmaraj S. Selenium and selenoproteins: it's role in regulation of inflammation. Inflammopharmacology. 2020; 28: 667-95.
15. Pecoraro BM, Leal DF, Frias-De-Diego A, Browning M, Odle J, Crisci E. The health benefits of selenium in food animals: a review. J Anim Sci Biotechnol. 2022; 13: 58.
16. Zhang Y, Cartland SP, Henriquez R, Patel S, Gammelgaard B, Flouda K, et al. Selenomethionine supplementation reduces lesion burden, improves vessel function and modulates the inflammatory response within the setting of atherosclerosis. Redox Biol. 2020; 29: 101409.
17. Zhou X, Zhao J, Cheng W, Chen S, Zhang Y, Qu Y, et al. Selenomethionine alleviates LPS-induced septic kidney injury by regulating mitochondrial dynamics changes. Front Pharmacol. 2025; 16: 1606365.
18. Meng T, He D, Han Z, Shi R, Wang Y, Ren B, et al. Nanomaterial-Based Repurposing of Macrophage Metabolism and Its Applications. Nanomicro Lett. 2024; 16: 246.
19. Xu Y, Wang Y, Guan L, Zhang P, Wu Z, Jehan S, et al. Precision Drug Delivery for Multifunctional Treatment of Abdominal Aortic Aneurysm Using Bioactive Tea Polyphenol Nanoparticles. ACS Appl Mater Interfaces. 2025; 17: 35080-98.
20. Benson TW, Conrad KA, Li XS, Wang Z, Helsley RN, Schugar RC, et al. Gut Microbiota-Derived Trimethylamine N-Oxide Contributes to Abdominal Aortic Aneurysm Through Inflammatory and Apoptotic Mechanisms. Circulation. 2023; 147: 1079-96.
21. Xu J, Zhao J, Chen H, Tan X, Zhang W, Xia Z, et al. Mesenchymal stromal cell-derived exosomes protect against abdominal aortic aneurysm formation through CD74 modulation of macrophage polarization in mice. Stem Cell Res Ther. 2024; 15: 242.
22. Zhang Y, Yan C, Dong Y, Zhao J, Yang X, Deng Y, et al. ANGPTL3 accelerates atherosclerotic progression via direct regulation of M1 macrophage activation in plaque. J Adv Res. 2025; 70: 125-38.
23. Yan H, Hu Y, Lyu Y, Akk A, Hirbe AC, Wickline SA, et al. Augmented expression of superoxide dismutase 2 mitigates progression and rupture of experimental abdominal aortic aneurysm. Theranostics. 2025; 15: 4016-32.